Tellus (1980), *32*, 410–427

Climatic-anomaly experiments in middle latitudes

By JOHN O. ROADS, *Climate Research Group, Scripps Institution of Oceanography, La Jolla, Ca. 92093, U.S.A.*

(Manuscript received January 3; in final form March 13, 1980)

ABSTRACT

A two-level spherical linear primitive-equation model is used to discuss the atmosphere's winter geopotential response to a localized heating in middle latitudes. It is shown that the response in the surface geopotential and potential temperature is largest for wave number one and decreases as the inverse of the zonal wave number for the next few waves. The response to heating has downstream warm lows and upstream cold highs and can be described simply as having zonal advection of temperature balancing the perturbation heating. Next, several low-order general-circulation-model anomaly experiments are run and compared to the linear model. It is shown that if the noise in the system is not too much larger than the linear solution or if the zonal state of the general circulation model is not close to linear resonance, linear theory can describe the time averaged results of the GCM.

1. Introduction

Long-lasting perturbations in the earth's surface conditions have been hypothesized by many researchers (see e.g. Namias, 1962) to force, through heating, anomalous responses in the atmospheric climate. The two major effects that have been studied are those due to anomalous snow and ice cover and sea-surface temperature anomalies (SSTAs). These hypotheses have spawned numerous studies with general-circulation models (GCMs). For example Spar (1973a), Williams and Washington (1974), Williams (1975), and Herman and Johnson (1978) studied the GCM response to anomalous snow and ice cover. Rowntree (1972, 1976a, 1976b), Spar (1973a, 1973b, 1973c), Houghton et al. (1974), Simpson and Downey (1975), Spar and Atlas (1975), Shukla (1975), Salmon and Hendershott (1975), Kutzbach et al. (1977), Huang (1978), and Julian and Chervin (1978) studied the GCM response to SSTAs. In addition, Washington (1972) has studied the effects due to thermal pollution produced by man.

Since the GCMs attempt to model the complex behaviour of the atmosphere, the response to certain simple forcings is complex. One of the major complexities is that the atmosphere and the GCMs have transient behavior and hence, considerable noise exists in time-averaged or ensemble-averaged solutions. Leith (1973), Chervin and Schneider (1976a, b) and Chervin et al. (1976) have suggested methods for determining the significance of GCM experiments in terms of individual grid points. However, since the effects of surface boundary conditions are usually small, the response in a GCM experiment is usually just barely significant. Moreover, it has recently been pointed out by Hasselmann (1978) that the response to these anomaly studies is typically what one might expect to occur by chance, namely 5% of the total grid points with a significance greater than 95%.

Hasselmann suggested that one way to increase the significance of the multivariate response was to have a reasonable first guess at the solution and that stationary linear theory might be used for this purpose. Egger (1977) also suggested that stationary linear theory might be used to physically understand the response, which, unless one has complete faith in the verisimilitude of the GCM, is all that one can really ask of these experiments. The response in these stationary models is easier to understand since there are no transient effects. Also, such models can be simplified to a point that

0040-2826/80/050410-18$02.50/0 © 1980 Munksgaard, Copenhagen

analytic understanding can be achieved through quasigeostrophic theory.

Stationary linear models linearize the time-averaged hydrodynamical equations about a basic zonal state and then solve for the stationary perturbations by standard algebraic techniques. Saltzmann (1968) presented a review on the subject and since then there have been studies by Sankar Rao (1970), Derome and Wiin-Nielsen (1971), Webster (1972), Egger (1976a, b), Vernekar and Chang (1978) and Ashe (1979) concerned mainly with explaining the observed stationary eddies in terms of orography and heating. In comparing the solutions of these models with the observed stationary eddies, one can conclude that the linear models are quite good and contain within them many of the mechanisms present in the general circulation.

Egger (1977) suggested that since the anomalous forcing due to anomalous boundary conditions was smaller than the average climatic forcing of the large-scale standing eddies, linear theory might even be more appropriate to anomaly studies. He then compared local responses between various GCM anomaly studies and his linear model.

In an attempt to make a more rigorous comparison, this study takes a non-linear semi-spectral spherical model and compares its time averaged solutions to a linear model. The forcing and friction are kept constant in both models, with the only difference between the models being that the non-linear and transient terms are absent from the linear model. It is shown that the stationary linear model can diagnose the time-averaged results of the time-dependent non-linear model except when the noise is much larger than the linear solution or when the GCM moves toward a state of linear resonance.

The models used in this study are described in Section 2. Section 3 discusses the response to an idealized heating source using the observed zonal averages. Section 4 discusses the results of some GCM experiments.

2. Models

The models are based upon the primitive equations of motion in spherical and pressure coordinates. The boundary conditions are that $\omega = 0$ at $p = 200$ mb and $w_s = \mathbf{v}_s \cdot \nabla H$. In the following equations:

u = zonal wind
v = meridional wind
$\mathbf{v}$ = vector wind (subscript s for surface)
θ = potential temperature
σ = static stability $= \frac{1}{2}\frac{\partial\theta}{\partial p}\Delta p$
φ = geopotential (subscript s for surface)
α_s = specific volume of air at surface
g = gravity
H = orographical heights
T_g = surface temperature
C_g = surface heat capacity
a = radius of sphere
$dx = a \cos d\lambda$ (λ is the longitude)
y = latitude
p = pressure ($2\Delta p$ is the increment of pressure over which integral is taken)
t = time
F_θ = potential temperature forcing
F_σ = static stability forcing
F_s = surface temperature forcing
τ = frictional stress
$\bar{A} = \frac{1}{2\pi}\int_0^{2\pi} A d\lambda$
$\hat{A} = A - \bar{A}$

The equations are divided into the zonal mean equations and the perturbation equations and may be written as:

A. Zonal equations

Zonal momentum

$$\frac{\partial \bar{u}}{\partial t} - f\bar{v} - \frac{\tan}{a} y\bar{u}\bar{v} + \nabla\cdot\bar{\mathbf{v}}\bar{u} + \frac{\partial\bar{\omega}\bar{u}}{\partial p} + g\frac{\partial}{\partial p}\bar{\tau}u$$
$$= \frac{\tan}{a} y\overline{\hat{u}\hat{v}} - \nabla\cdot\overline{\hat{\mathbf{v}}\hat{u}} - \frac{\partial}{\partial p}\overline{\hat{\omega}\hat{u}}$$

Meridional momentum

$$\frac{\partial\bar{v}}{\partial t} + f\bar{u} + \frac{\tan}{a} y\bar{u}^2 + \frac{1}{a}\frac{\partial\theta}{\partial y} + \nabla\cdot\bar{\mathbf{v}}\bar{v} + \frac{\partial}{\partial p}\bar{\omega}\bar{v}$$
$$+ g\frac{\partial}{\partial p}\bar{\tau}_v = \frac{-\tan}{a} y\overline{\hat{u}^2} - \nabla\cdot\overline{\hat{\mathbf{v}}\hat{\mathbf{v}}} - \frac{\partial}{\partial p}\overline{\hat{\omega}\hat{v}}$$

Layer-averaged potential temperature

$$\frac{\partial\hat{\theta}_m}{\partial t} + \int_{2\Delta p}\left(\nabla\cdot\bar{\mathbf{v}}\bar{\theta} + \frac{\partial}{\partial p}\bar{\omega}\bar{\theta}\right)\frac{dp}{2\Delta p} - g\frac{\partial}{\partial p}\bar{F}_\theta$$
$$= -\int_{2\Delta p}\left(\nabla\cdot\overline{\hat{\mathbf{v}}\hat{\theta}} + \frac{\partial}{\partial p}\overline{\hat{\omega}\hat{\theta}}\right)\frac{dp}{2\Delta p}$$

Layer static stability

$$\frac{\partial\bar{\sigma}}{\partial t}+\frac{1}{2}\frac{\partial}{\partial p}\left(\nabla\cdot\bar{\mathbf{v}}\bar{\theta}+\frac{\partial}{\partial p}\bar{\omega}\bar{\theta}\right)\Delta p-g\frac{\partial}{\partial p}\bar{F}_{\sigma}=-\frac{1}{2}\frac{\partial}{\partial p}\left(\nabla\cdot\overline{\hat{\mathbf{v}}\hat{\theta}}+\frac{\partial}{\partial p}\overline{\hat{\omega}\hat{\theta}}\right)\Delta p$$

Surface geopotential

$$\frac{\partial\bar{\phi}_s}{\partial t}+\bar{\mathbf{v}}_s\cdot\nabla(\bar{\phi}-g\bar{H})-\bar{\omega}_s\bar{\alpha}_s=-\overline{\hat{\mathbf{v}}_s\cdot\nabla(\hat{\phi}_s-g\hat{H})}-\overline{\hat{\omega}_s\hat{\alpha}_s}$$

Ground temperature

$$\frac{\partial\bar{T}_g}{\partial t}-\overline{C_g^{-1}}\,\overline{F_s}=\overline{\hat{C}_g^{-1}\hat{F}_s}$$

B. Perturbation equations

Zonal momentum

$$\frac{\partial\hat{u}}{\partial t}-f\hat{v}-\frac{\tan}{a}y(\bar{u}\hat{v}+\hat{u}\bar{v})+\frac{\partial\hat{\phi}}{\partial x}+\nabla\cdot(\bar{\mathbf{v}}\hat{u}+\hat{\mathbf{v}}\bar{u})+\frac{\partial}{\partial p}(\bar{\omega}\hat{u}+\hat{\omega}\bar{u})+g\frac{\partial}{\partial p}\hat{\tau}_u=\frac{\tan}{a}y\widehat{\hat{u}\hat{v}}-\nabla\cdot\widehat{\hat{\mathbf{v}}\hat{u}}-\frac{\partial}{\partial p}\widehat{\hat{\omega}\hat{u}}$$

Meridional momentum

$$\frac{\partial\hat{v}}{\partial t}+f\hat{u}+\frac{\tan}{a}y(2\bar{u}\hat{u})+\frac{1}{a}\frac{\partial\widehat{\phi}}{\partial y}+\nabla\cdot(\bar{\mathbf{v}}\hat{v}+\hat{\mathbf{v}}\bar{u})\hat{\nabla}+\frac{\partial}{\partial p}(\bar{\omega}\hat{v}+\hat{\omega}\bar{v})+g\frac{\partial}{\partial p}\hat{\tau}_v=-\frac{\tan}{a}y\widehat{\hat{u}\hat{u}}-\nabla\cdot\widehat{\hat{\mathbf{v}}\hat{v}}-\frac{\partial}{\partial p}\widehat{\hat{\omega}\hat{v}}$$

Layer-averaged potential temperature

$$\widehat{\frac{\partial\theta_m}{\partial t}}+\int_{2\Delta p}\left(\nabla\cdot(\bar{\mathbf{v}}\hat{\theta}+\hat{\mathbf{v}}\bar{\theta})+\frac{\partial}{\partial p}(\bar{\omega}\hat{\theta}+\hat{\omega}\theta)\right)\frac{dp}{\Delta p}-g\frac{\partial}{\partial p}\hat{F}_{\theta}=-\int_{2\Delta p}\left(\nabla\cdot(\widehat{\hat{\mathbf{v}}\hat{\theta}})+\frac{\partial}{\partial p}(\hat{\omega}\hat{\theta})\right)\frac{dp}{2\Delta p}$$

Layer static stability

$$\frac{\partial\hat{\sigma}}{\partial t}+\frac{1}{2}\frac{\partial}{\partial p}\left(\nabla\cdot(\bar{\mathbf{v}}\hat{\theta}+\hat{\mathbf{v}}\bar{\theta})+\frac{\partial}{\partial p}(\bar{\omega}\hat{\theta}+\hat{\omega}\bar{\theta})\right)\cdot\Delta p-g\frac{\partial}{\partial p}\hat{F}_{\sigma}=-\frac{1}{2}\frac{\partial}{\partial p}\left(\nabla\cdot(\widehat{\hat{\mathbf{v}}\hat{\theta}})+\frac{\partial}{\partial p}\widehat{\hat{\omega}\hat{\theta}}\right)\Delta p$$

Surface geopotential

$$\frac{\partial\hat{\phi}_s}{\partial t}+\bar{\mathbf{v}}_s\cdot\nabla\hat{\phi}_s+\hat{\mathbf{v}}_s\cdot\nabla(\bar{\phi}_s-g\bar{H})-\bar{\omega}_s\hat{\alpha}_s-\hat{\omega}_s\bar{\alpha}_s=\bar{\mathbf{v}}_s\cdot\nabla g\hat{H}-\hat{v}_s\cdot\nabla\widehat{\hat{\phi}_s-g\hat{H}}-\widehat{\hat{\omega}_s\hat{\alpha}_s}$$

Ground temperature

$$\frac{\partial\hat{T}_g}{\partial t}-\bar{C}_g^{-1}\hat{F}_s=\hat{C}_g^{-1}\bar{F}_s+\widehat{\hat{C}_g^{-1}\hat{F}_s}$$

These equations are then finite differenced in the vertical into two levels with u and v carried at the upper (1) and lower (2) levels, ω carried at the middle (3/2) and surface level (s), θ and σ carried at the middle level and θ_s carried at the surface level. The following interpolation and extrapolation schemes are used to define model variables at those levels at which they are not carried.

$$\mathbf{v}_s=\mathbf{v}_2/2$$
$$\mathbf{v}_{3/2}=(\mathbf{v}_1+\mathbf{v}_2)/2$$
$$\theta_s=\theta_m-2\sigma$$
$$\theta_1=\theta_m+\sigma$$
$$\theta_2=\theta_m-\sigma$$

The vertical velocities are determined from the divergence equation.

$$\omega=-\nabla\cdot\mathbf{v}_1\Delta p$$
$$\omega_s=\omega-\nabla\cdot\mathbf{v}_2\,\Delta p$$

The geopotentials are determined by the requirement that the horizontally averaged equations conserve total energy plus kinetic energy and are hydrostatic (see Arakawa and Mintz, 1974). Therefore,

$$\phi_1=\alpha_1\,\theta+\beta\sigma+\phi_s\quad \alpha_1\sim 2.3\times 10^2\ \mathrm{m^2\,s^{-2}\,K^{-1}}$$
$$\phi_2=\alpha_2\,\theta+\beta\sigma+\phi_s\quad \alpha_2\sim 6.0\times 10^1\ \mathrm{m^2\,s^{-2}\,K^{-1}}$$
$$\alpha_s=(\alpha_3\,\theta+\beta_3\,\sigma)R/p\beta\sim -1.0\times 10^2\ \mathrm{m^2\,s^{-2}\,K^{-1}}$$
$$\alpha_3\sim 0.9$$
$$\beta_3\sim -1.9$$

The heating terms F_θ, F_σ and F_s are taken from Smagorinsky (1962) and are described in more detail in Appendix I, along with the friction parameterization for τ.

These equations are finite differenced in the meridional direction using Kurihara's (1967) finite difference scheme. Only the northern hemisphere is used and hence mirror-boundary conditions at the equator are used. By judiciously choosing the grid points, the northern boundary condition is that $A(y) \cos y \to 0$ as $\cos y \to 0$.

All variables are expanded zonally in a Fourier series of the form $A = \bar{A} + \sum_{n=1}^{N} a_n \cos n\lambda + \sum_{n'=1}^{N} a'_{n'} \sin n'\lambda$. Since, the major interest in this paper is a model where N is small, all non-linear combinations are calculated via interaction coefficients $(c_{nn'l})$. For example,

$$\hat{A}\hat{B}_l = \sum_{n=1}^{N} \sum_{n'=1}^{N} a_n b_{n'} c_{nn'l} + \cdots$$

These coefficients are easily evaluated analytically.

The time differencing of the GCM is done with a leap-frog scheme with periodic insertion of an Euler-backward step (every twelve steps) in order to damp the computational mode and gravity waves (see Kurihara, 1965). As is usual, the forcing and friction terms are evaluated at a previous time step.

The time-dependent solution is also smoothed in the meridional direction every time step by means of a high-order filter (see Shapiro, 1970; Francis, 1975). This filter is equivalent to a high-order diffusion operator of the form ∇^m and acts to eliminate two grid-point waves, while leaving the larger waves virtually unaffected. The model becomes unstable if no smoothing is done, presumably because of the aliasing of two grid-point waves (see Haltiner, 1971). No smoothing, except for the removal of the wave numbers greater than six at the northernmost grid point, is done in the zonal direction.

The difference between the GCM and the linear model is represented schematically below. A more detailed comparison is given in Appendix II. First, the GCM calculates the zonal solution. This zonal solution is used in the perturbation equations as a matrix operator B. The perturbation equation is:

$$\frac{\partial \hat{x}}{\partial t} = \underbrace{-\bar{B}\hat{x}}_{\text{linear}} + \underbrace{\hat{X}}_{\text{heating, orography}} \underbrace{- \sum \sum \widehat{\hat{c}\hat{x}}}_{\text{non-linear}}.$$

Averaging over a long time (the averaging operator is denoted by overhead $\sim$) gives

$$\frac{\partial \tilde{\hat{x}}}{\partial t} = - \widetilde{\bar{B}\hat{x}} + \tilde{\hat{X}} - \sum \sum \widetilde{\widehat{\hat{c}\hat{x}}}$$

The linear model is

$$0 = -\tilde{\bar{B}}\tilde{\hat{x}} + \tilde{\hat{X}}$$

Thus, the differences in the solutions are due to the terms $-\widetilde{\bar{B}'\hat{x}'} - \sum\sum \widetilde{\hat{c}'\hat{x}'} - \sum\sum \widehat{\tilde{\hat{c}}\tilde{\hat{x}}} - \partial\tilde{\hat{x}}/\partial t$, which are composed of the linear and non-linear transient eddy fluxes and the average time dependence.

For the comparisons in this paper, the models are run with the heating and friction coefficients kept constant in order to make the differences dependent only upon the transient and stationary-eddy flux terms. To make the comparison as accurate as possible, all model variables are averaged continuously; hence, there is no sampling error.

3. Linear model experiments with observed zonal state

A theoretical linear response to an idealized forcing field for the potential temperature is now studied. The forcing is a point-source cooling placed in the center of the domain. Only the mean potential temperature is forced. This function is expanded into a Fourier cosine series (the sine series is zero) and is shown in Fig. 1 as a function of wave number. Of course, the values are quantized with discrete wave numbers; the continuous lines are drawn in order to help the reader easily see the values. The total cooling as a function of the zonal coordinate for six waves, is shown on the right. With a point source, all wavelengths are present with equal amplitudes, albeit with phase differences of 180°. That is, $A_n = (1/\pi) \int^{2\pi} \delta_0 \cos n\lambda \, d\lambda \equiv -1 \times 10^{-6} \cos n\lambda_0$ K s^{-1}. It is assumed that $\delta_0 \, d\lambda \to -\pi \times 10^{-6}$ as $\lambda + |d\lambda| \to \lambda_0$. The reason for showing this Fourier expansion of a point source is to point out how misleading it is to assume that a small-scale isolated response is described only by small-scale waves. In fact, all wave amplitudes are influenced equally, although with different phases. The response of a system to a point source will be isolated only if all waves are excited equally and have alternating phases. This is

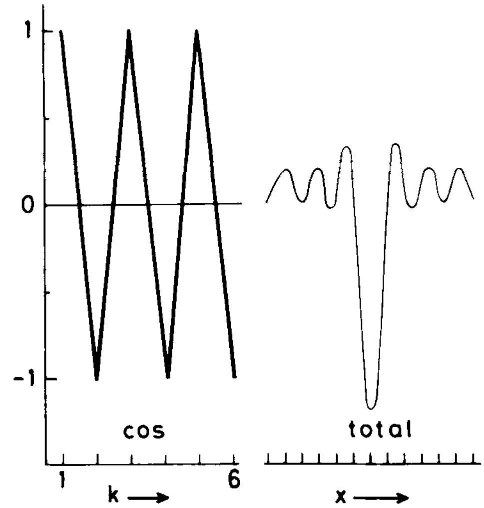

Fig. 1. The Fourier cosine expansion of a delta function cooling placed in the center of the domain (middle latitudes) as a function of wave number b. The total representation as a function of x is shown on the right-hand side. The heating wave amplitudes are in 10^{-6} K s^{-1}. The total heating is in arbitrary units.

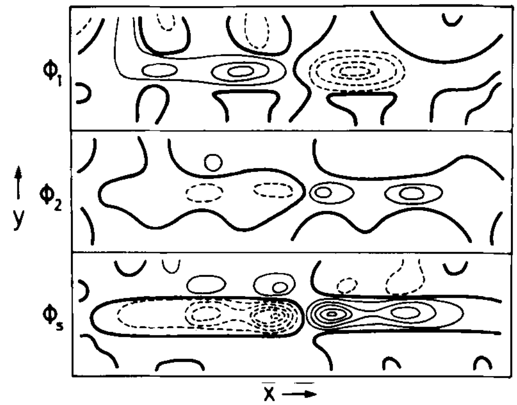

Fig. 2. The total response for the midlatitude δ cooling for ϕ_1, ϕ_2 and ϕ_s. The contours are every 2.5 gpm. The solid lines are the positive values, the dashed lines the negative values and the heavy line is the zero line.

not the case for the observed winter zonal state, as will be discussed in the remainder of this section.

The total response to the point source in a truncated linear model (5 meridional grid points, 6 zonal waves) which uses the observed winter zonal state (see Fig. 5) is shown in Fig. 2. At the lower level the delta cooling induces downstream highs and upstream lows. At the upper level, the situation is reversed with downstream lows and upstream highs. The solution predominantly affects middle latitudes. The amplitude is strongest at the surface, with a maximum on the order of 13 m; the amplitude decreases with elevation and then increases once again in the high altitudes to a maximum of around 11 m, with a change of phase of 180°.

To understand this response, asymptotic solutions from frictionless linear quasigeostrophic theory are considered. A linear two-level model taken from Holton (1972) is shown below.

$$ik(\beta - u_1 \alpha^2)\, \psi_1 = \frac{f}{\Delta p}\, \omega$$

$$ik(\beta - u_2 \alpha^2)\, \psi_2 = -\frac{f}{\Delta p}\, \omega$$

$$-\omega + \frac{\Delta p}{f_0} \lambda^2 ik \left(\frac{u_1 + u_2}{2} (\psi_1 - \psi_2) + \frac{(\psi_1 + \psi_2)}{2} (u_2 - u_1) \right) = \lambda^2 (\alpha_1 - \alpha_2) \dot{F} \frac{\Delta p_2}{f_0}$$

where

$$\beta = \frac{\partial f}{\partial y}$$

$$\lambda^2 = f^2/(\sigma(\alpha_1 - \alpha_2))$$

$$\dot{F} = \frac{d\theta}{dt}$$

$\alpha^2 = k^2 + l^2$: vector wave number squared

$\alpha_1 = 2.3 \times 10^2$ m^2 s^{-2} K^{-1}

$\alpha_2 = 6 \times 10^1$ m^2 s^{-2} K^{-1}

Substituting the relations

$$f\psi_1 = \alpha_1 \theta + \phi_s$$

$$f\psi_2 = \alpha_2 \theta + \phi_s$$

results in the model equations

$$\theta\{\alpha_1 \beta - u_1 \alpha^2 \alpha_1 - A\} + \phi_s\{\beta - u_1 \alpha^2 - A'\} = i\lambda^2(\alpha_1 - \alpha_2)\, \dot{F} k^{-1}$$

$$\theta\{\alpha_2 \beta - u_2 \alpha^2 \alpha_2 + A\} + \phi_s\{\beta - u_2 \alpha^2 + A'\} = -i\lambda^2(\alpha_1 - \alpha_2)\, \dot{F} k^{-1}$$

where

$$A = \lambda^2(u_2\,\alpha_1 - u_1\,\alpha_2)$$

$$A' = \lambda^2(u_2 - u_1)$$

The solution for θ and ϕ_s is

$$\theta = \frac{i\lambda^2}{kD}(\alpha_1 - \alpha_2)\,\hat{F}(2\beta - \alpha^2(u_1 + u_2))$$

and

$$\phi_s = \frac{-i\lambda^2}{kD}(\alpha_1 - \alpha_2)\,\hat{F}(\beta(\alpha_1 + \alpha_2) - \alpha^2(u_1\,\alpha_1 + u_2\,\alpha_2))$$

where

$$D = (\alpha_1\,\beta - u_1\,\alpha^2\,\alpha_1 - A)(\beta - u_2\,\alpha^2 + A') - (\beta - u_1\,\alpha^2 - A')(\beta\alpha_2 - u_2\,\alpha^2\,\alpha_2 + A)$$

Although this gives relatively simple formulas for determining the response, the values are still not readily apparent. Therefore, assymptotic values are derived for the ultralong waves ($\beta \gg u\alpha^2$) and for the long waves ($\beta \ll u\alpha^2$). Salzman (1968) discusses these waves.

Case 1: $u\alpha^2 \ll \beta$ (ultralong wave approximation)

The ratio

$$\frac{\theta}{\phi_s} \to -\frac{2}{(\alpha_1 + \alpha_2)} = -0.69 \times 10^{-6}$$

That is, θ is 180° out of phase with ϕ_s. Also, 1 gpm in ϕ_s occurs for every 0.07 K in θ. Since $\phi_1 = \alpha_1\,\theta + \phi_s$ and $\phi_2 = \alpha_2\,\theta + \phi_s$, ϕ_1 is out of phase with ϕ_s and ϕ_s is in phase with ϕ_s, but reduced in amplitude. Calculating the amplitudes

$$\theta \approx \frac{i\lambda^2(\alpha_1 - \alpha_2)\,2\beta\hat{F}}{k\{(\alpha_1\,\beta - A)(\beta + A') - (\beta - A')(\beta\alpha_2 + A)\}}$$

The asymptotic solution is

$$\theta \approx -i \times \frac{4.9 \times 10^5\,\hat{F}}{k'}$$

where k' is the integral zonal wave number. Since $\lambda^2\,u > \beta$, the solution is approximately

$$\theta \approx -\frac{i \times 2\hat{F}}{k(u_2 + u_1)}$$

That is, the heating is balanced mainly by the mean zonal advection; the mean meridional advection is zero and the adiabatic heating is small.

Case 2: $u\alpha^2 \gg \beta$ (long wave approximation)

$$\frac{\theta}{\phi_s} \to -\frac{(u_1 + u_2)}{(u_1\,\alpha_2 + u_2\,\alpha_2)} = 5.7 \times 10^{-7}$$

Again θ and ϕ_s are 180° out of phase, and 1 gpm in ϕ_s occurs for every 0.06 K in θ. Calculating the amplitude for this case gives

$$\theta \to -\frac{i\lambda_2^2\,\hat{F}}{k\alpha^2}\,\frac{(u_1 + u_2)(\alpha_1 - \alpha_2)}{u_1\,u_2(\alpha_1 + \alpha_2)}$$

Physically, the response of the system can be understood through the thermodynamic equation:

$$\omega - \frac{\omega\lambda^2}{(\beta - u_m\,\alpha^2)}\left(u_2^2\,\frac{(\beta - u_m\,\alpha^2)}{(\beta - u_1\,\alpha^2)} + u_1\,\frac{(\beta - u_m\,\alpha^2)}{(\beta - u_2\,\alpha^2)}\right) = -\frac{\hat{F}}{\sigma}\,\Delta p$$

The first ω term on the left-hand side is the adiabatic heating and cooling and the second term is the horizontal advection.

For the ultralong waves ($u\alpha^2 \ll \beta$), the dominant term is the advection term, since $\lambda^2\,u > \beta$. This advection term is large since small changes in the vertical velocity induce large changes in the geopotentials through the divergence term. Thus for the ultralong waves in middle latitudes, advection balances the diabatic and adiabatic heating. There is a k^{-1} dependence for the amplitudes of the pressure and temperature on the heating and a k dependence of the vertical velocity with respect to temperature and pressure. For the long waves ($u\alpha^2 \gg \beta$), the dominant term is the adiabatic term which balances the advection and the diabatic heating. There is a $k^{-1}\,\alpha^{-2}$ dependence for the amplitudes of pressure and temperature on heating and a $k^1\,\alpha^2$ dependence of vertical velocity on pressure and temperature for this case.

In each of these limits, the pressure configuration is the same—warm lows downstream and cold highs upstream of the heating. The vertical velocity is downward over the heating for the ultralong waves and upward over the heating for the long waves.

Diabatic and adiabatic heating are balanced by advection for the ultralong waves. Diabatic heating and advection of temperature are balanced by adiabatic cooling for the long waves. Resonance in the system, that is all amplitudes approach infinity, occurs when adiabatic cooling balances the advection of temperature and the system is unable to balance the diabatic heating. It is near the resonance point that linear theory is probably least valid, but where the amplitude can be very large and so one should have clear idea where it occurs for a particular model. Resonance occurs when:

$$0 = (\beta - u_1\,\alpha^2)\,(\beta - u_2\,\alpha^2) - \lambda^2\,u_1(\beta - u_1\,\alpha^2) - \lambda^2\,u_2(\beta - u_2\,\alpha^2)$$

Solutions for this have been discussed extensively by Egger (1976). For the winter parameters for λ^2, u_1, u_2, this gives a value at 45° latitude for α^2 of 9×10^{-17} cm^{-2}. For $l = 0$, this falls between zonal wave numbers 4 and 5, and as l increases the resonant zonal wavenumber decreases. A suitable approximation to resonance in this model is $\alpha^2 = \beta/u_1 \sim 1 \times 10^{-16}$ cm^{-2}, since $\lambda^2 u_1(\beta - u_1\,\alpha^2)$ is the dominant term for the ultralong waves. At resonance the model response is determined by the damping terms in the equation. Thermal damping coefficients are presumably the largest dampers; this is due mainly to sensible and latent heat transfer from the surface. These thermal damping coefficients were not included in the frictionless quasigeostrophic theory in order to facilitate the analysis. However, at resonance, the solutions are particularly simple and can be obtained by omitting the dynamical terms and substituting the frictional and thermal damping terms. Near-resonant solutions, in which all terms become important, are more complicated and will be discussed in subsequent papers.

The linear primitive equation model response in middle latitudes as a function of wave number is compared to quasigeostrophic theory and is shown in Fig. 3. The cosine response is shown on the left-hand side and the sine response on the right-hand side. The cosine response is induced in quasigeostrophic theory from friction which is usually small for the ultralong waves compared to the other terms. In the primitive equations, the cosine response is also induced due to terms like $\bar{v}(\partial\bar{\theta}/\partial y)$, etc. The decreasing sine wave is taken from the linear primitive equation model whereas the envelope lines are taken from frictionless quasigeostrophic theory for the ultralong wave approximation. The other envelope lines are the longwave approximation. The phases are not noted

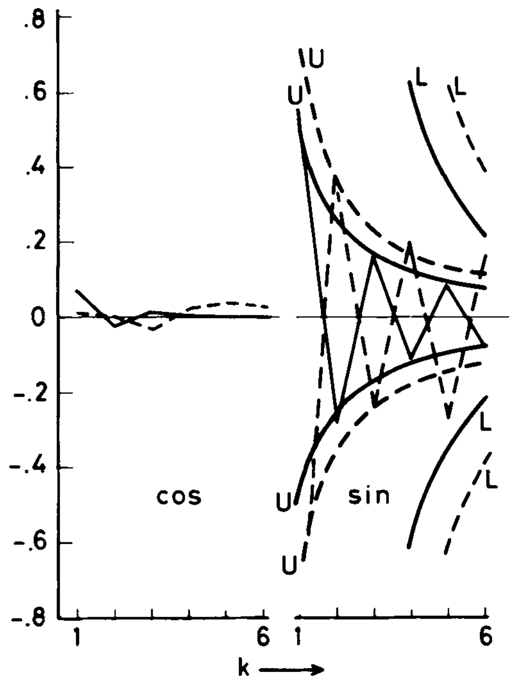

Fig. 3. The response in middle latitudes of the potential temperature, solid line, and the surface geopotential, dashed line, to the delta function as a function of k. The cosine response is shown on the left-hand side and the sine response on the right-hand side. The ordinate values are plotted in 0.1 K for the temperature and 1 gpm for surface geopotential. Quasigeostrophic theory for the ultralong waves gives the envelope curves (labeled U) to the linear model response. The curves labeled L are the longwave approximations which assume that the meridional wavelength is 90°. The solid lines are the potential temperature response and the dashed lines are the surface geopotential response. The phases are not drawn for quasigeotrophic theory but are the same as for the primitive equation model.

from quasigeostrophic theory on the figure although the previous case studies indicated that the same phases are present; that is, the positive potential temperature is upstream from the heating by 90°. Note that for the most part, the solution can be described by the ultralong waves. This is verified by looking at the vertical velocity response. There is also a decrease in θ and ϕ_s proportional to k^{-1}. Similar results were obtained by Derome and Wiin-Nielsen (1971) for the largest waves. Also note that the only sign of resonance in the system is the larger amplitude surface pressure response near wave number 5.

Comparing Fig. 3 with Fig. 2 one sees that for the values of the parameters in the system, a middle-latitude point cooling will induce downstream highs and upstream lows at the lower levels, a reversal at high altitudes, and a node in the middle levels of the atmosphere. Essentially, the wave response has warm lows ahead and cold highs behind a middle latitude heating, with the total response dependent upon the configuration of the imposed heating.

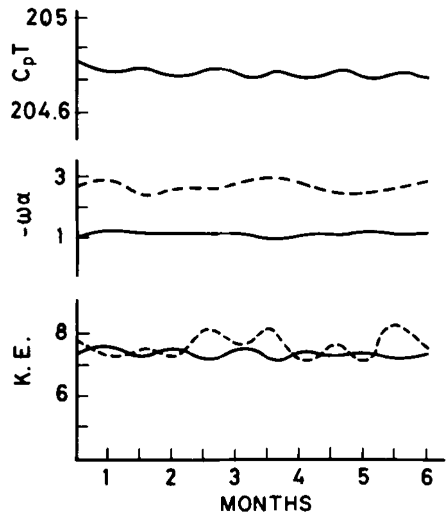

Fig. 4. Time series for the GCM run of six months. Points are plotted from two-week averages and four weeks are denoted as one unit. The upper line shows the total potential energy (TPE) in units of 10^7 J m^{-2}; the next two lines show the conversion from TPE to eddy kinetic energy $(-\omega\alpha)$ and from TPE to zonal kinetic energy $(-\bar{\omega}\alpha)$ in units of 1 J m^{-2} s^{-1}; the bottom two lines show the eddy kinetic energy (EKE) on the dashed curve and zonal kinetic energy (ZKE) on the solid line in units of 10^5 J m^{-2}.

4. GCM runs

In the subsequent sections, three major GCM runs are described. Each run consists of several experiments of 1 month and each run compares its monthly averages to the linear primitive equation model. These runs differ either in the number of waves and meridional grid points or in the values of the perturbation heating that are used.

4.1. *First GCM run*

In the first GCM run, the number of grid points and the number of zonal waves were kept the same as that in Section 3. In order to make the comparison between the linear model and the GCM as accurate as possible, it was decided to run the GCM for a sufficiently long, fixed winter simulation. It was also decided to make the heat capacity of the surface constant and appropriate to a 10 cm swamp. Also, the heating and friction coefficients were kept constant. It was not expected that this model would necessarily produce completely realistic features, but rather features that would be produced by a circulation near to the parameter range of a winter climate and that could be easily compared to the linear model.

Time series of the total potential energy, kinetic energies and conversion time for the last six months of the control run (no perturbation heating) are shown in Fig. 4 (points are plotted from two-week averages). The values tend to be somewhat realistic although the eddy kinetic energy and conversion term tended to be larger than the observed averages. Also, there tends to be a direct conversion of zonal-available-potential energy to zonal-kinetic energy.

As shown in Fig. 5, the magnitudes of the various zonal variables seem to compare qualitatively to the earth's winter parameters. It is important to remember that the simulation is run for a fixed winter on a hemisphere, whereas the natural circulation goes through a seasonal cycle on the sphere. For example, the zonal wind at the upper level tends to be of the same magnitude as the observed in middle latitudes; however, it is too large and the maximum is further north than the observed. This is related to the stronger tem-

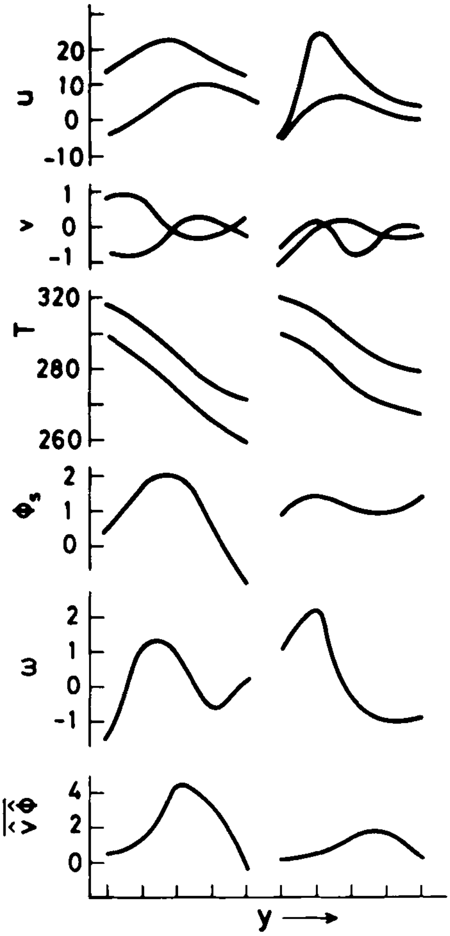

Fig. 5. Zonal averages for the GCM are plotted on the left-hand side of the figure and the observed values for winter are plotted on the right-hand side of the figure. The first two lines are the upper (u_1) and lower (u_2) level zonal wind plotted in ms^{-1}; the next two lines are the upper (v_1) and lower (v_2) level meridional wind in ms^{-1}; the third set of lines are the potential temperature (θ) and ground temperature (T_g) in K: the next line is the 1000 mb geopotential (ϕ_s) in values of 10 gpm; the next line is the pressure velocity at 600 (ω) in units of 10^{-2} kg m^{-1} s^{-3}; the final line shows the zonally averaged perturbation meridional transport of potential temperature ($\overline{\hat{v}\hat{\theta}}$) in units of m K s^{-1}. The observed is the meridional transport of sensible heat $\overline{\hat{v}\hat{T}}$ which is almost the same as $\overline{\hat{v}\hat{\theta}}$.

perature and surface geopotential gradients. The presence of the more regular Hadley cells is due to confining the circulation to the hemisphere. Finally, Fig. 5 shows that the fixed winter simulation has an

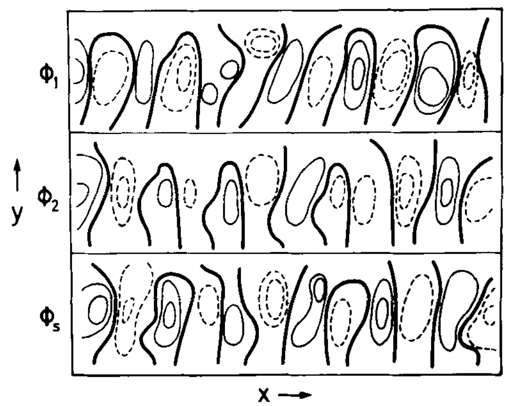

Fig. 6. A typical instant in the GCM run for $\hat{\phi}_1$, $\hat{\phi}_2$, and $\hat{\phi}_s$. The contours are drawn every 100 gpm for $\hat{\phi}_1$, and every 50 gpm for $\hat{\phi}_2$ and $\hat{\phi}_s$. The solid, dashed and heavy lines have the same meaning as in Fig. 2.

increased eddy transport of a sensible heat. There are no indications that the level of truncation has drastically affected the zonal averages.

A "typical" synoptic situation is shown in Fig. 6 for this model for the upper and lower levels and surface. The model tends to be dominated by wave number six in middle latitudes and wave number three in high latitudes and, as in the stationary model, has warm lows and cold highs. There is a pronounced westward tilt of the eddies and the amplitudes are quite strong (i.e. at 400 mb the amplitudes approach 300 m). The amplitudes are weaker at the surface although surface pressure variations are still on the order 10–20 mb.

The GCM has instabilities in middle latitudes at the high wave numbers and less instability at the low wave numbers and thus should be well described by linear theory. The dominance of the high wave numbers is a major defect in the model if its solutions are to be compared to the observed, but an asset in that it allows a good test as to how well the linear model can diagnose the linear state in the GCM.

The experiment that will next be discussed is concerned with the point-source cooling described in Section 3. This cooling is first inserted into the linear model at the midpoint; only the perturbation cooling is included. Fig. 7 shows the total response in the primitive-equation linear model to this forcing. The zonal state for the linear model was

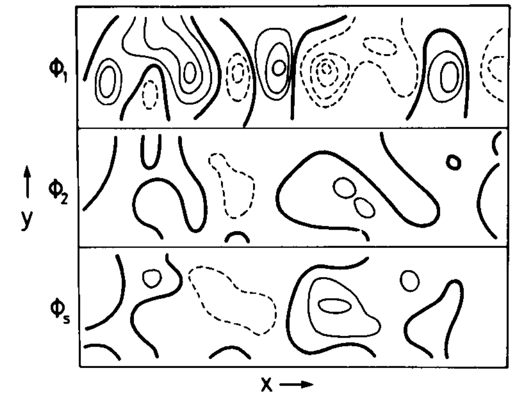

Fig. 7. Same as Fig. 2 except that the linear model, which is the counterpart to the GCM, is used along with the zonal state of the GCM.

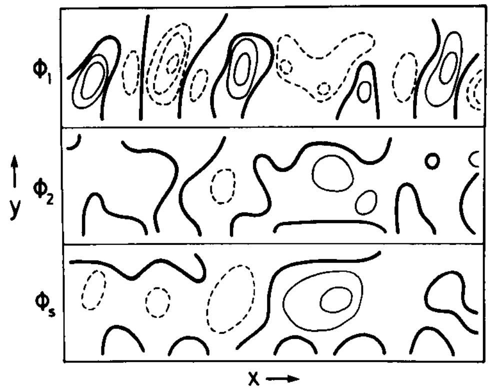

Fig. 8. Same as Fig. 7 except for the difference between the anomaly run and the control run of the GCM. Also, the contours are drawn every 7.5 gpm since a point source three times as large as that for Fig. 7 was used.

taken from the GCM control run. Also, the horizontal smoothing term from the GCM was incorporated into the linear model. The response is reduced considerably compared to that in Fig. 2, due to the inclusion of the horizontal smoothing and the heating feedback terms and the larger mean zonal wind that the GCM produces. Also, note that the response is not so isolated in middle latitudes; this is also due to the horizontal smoothing which eliminates two grid-point waves. Still, the response is qualitatively similar to the response in Section 3—cold highs downstream and warm lows upstream from the cooling.

The GCM anomaly run is now compared to this linear model. The anomaly run was initialized two weeks after the start of the control run, the anomalous heating inserted, and the model run for 8 days. The model was then run for an additional 4 weeks. The six-month average of the control run was subtracted from this anomalous four-week average and the differences are shown in Fig. 8. The anomalous heating for each wave in middle latitudes was increased to 3×10^{-6} K in order to make sure that the result would be easily detected above the noise.

This type of heating can easily be associated with anomalous sea-surface temperatures. For example, the transfer of heat from the surface is $p_s C_D |\mathbf{v}_s| (T_g - T_s)(1 + (L/C_p)(\partial q^*/\partial T)) = F_s$ and the heating of the troposphere $d\theta/dt$ is $(g/2\Delta p)(p_0/p)^{\kappa} F_s$. A "typical" value is 7×10^{-6} $(T_g - T_s)$; therefore changes of less than a degree Celsius in ocean temperatures are appropriate to these heating values.

Fig. 8 shows the response in the GCM to the anomalous heating. The response is quite similar to the linear model. There are cold highs downstream and warm lows upstream from the cooling; the amplitudes are about the same and the phases are qualitatively similar. Note that the contours are every 7.5 gpm instead of 2.5 gpm since the heating was three times as strong in the GCM as it was in the linear model. For the linear model, the amplitudes would, of course, increase three times as much for a heating three times as strong.

Figs. 9 and 10 show the comparison as a function of wave number in middle latitudes. First, Fig. 9 shows the linear-model response for a heating of 3×10^{-6} Ks^{-1} for each wave. The results are comparable to those in Fig. 3, with a large amplitude wave number 1 response and a subsequent reduction in amplitude with increasing wave number. However, there seems to be a much stronger (i.e. resonant) response in the temperature field near wave number 5 than was present in the model in Section 3. Also, the amplitudes are reduced by factors of 2 or 3, again because of heating feedbacks and horizontal smoothing.

The difference response is shown in Fig. 10. Note that for the most part the response compares well with Fig. 9, with the exception of wave number 6. Even the response near resonance is well represented. The error bars, which indicate plus or

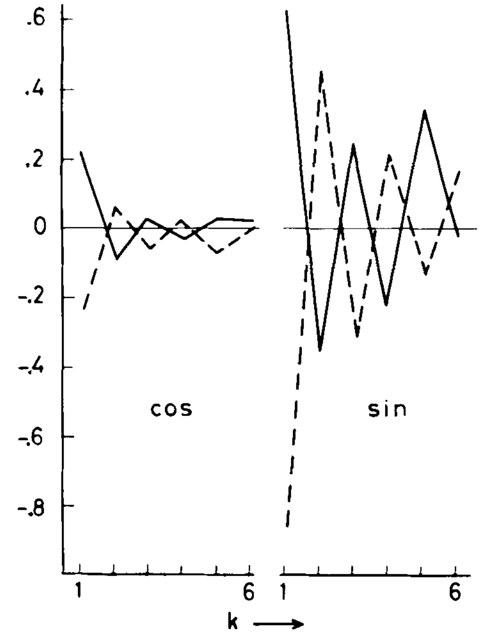

Fig. 9. Same as Fig. 3 except for the linear counterpart to the GCM and a point source three times as large.

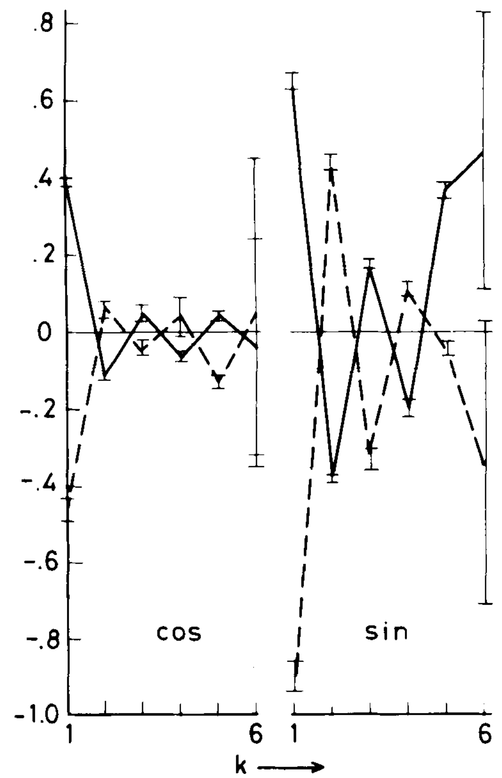

Fig. 10. Same as Fig. 9 except that this is the difference between the anomaly run and the control run with the GCM. Also, the standard deviations of monthly averages (± 1 standard deviation) are shown by the error bars for wave number.

minus 1 standard deviation of monthly averages, show why the total comparison can be worse. Because of strong temporal changes in wave number 6, presumably due to baroclinic instability, the averages in the smallest scale show strong deviations and meaningful comparisons cannot be made between stationary linear theory and monthly differences for the high wave numbers. However, the comparison seems quite good for the low wave numbers. Thus for low-order time-dependent models, stationary linear theory can predict anomalous responses for the largest waves. However, since the model is so highly truncated, non-linear influences of the smaller-scale waves are absent.

4.2. *Second GCM run*

It was for this reason that the general circulation model was made more realistic by increasing the number of meridional grid points and the number of horizontal waves. Fig. 11 shows a time series of the zonal and eddy kinetic energies (plotted every 10 days) for a state initialized with a zonal state consisting of a zonal wind and a meridional temperature gradient. The meridional grid distance was 11.25° and only waves 3 and 6 were allowed initially. The perturbation heating was changed to give an amplitude in the cosine wave of -2.4×10^{-6} K s^{-1} for wave 3 and $+2.4 \times 10^{-6}$ K s^{-1} for wave 6 at gridpoints 4 and 5. The perturbation heating was set to zero elsewhere. After 30 days wave number 6 had eddy kinetic energies on the order of 10^9 ergs cm^{-2} s^{-1} and wave 3 had kinetic energies of only 10^6 ergs cm^{-2} s^{-1}. Therefore, the low kinetic energy in this wave did not seem to be related to the number of meridional grid points. On the second 30 days, the number of horizontal waves was increased to include wavenumbers 9 and 12. Immediately, the eddy kinetic energy in wave 3 increased. Because of the noise that was then

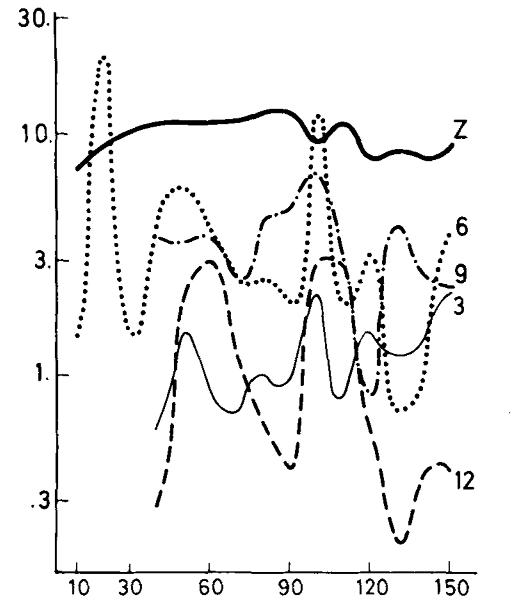

Fig. 11. Time series (taken from points 10 days apart) of the zonal kinetic energy, *z*, and eddy kinetic energy for wave numbers 3, 6, 9, 12 in units of 10^5 J m^{-2} as a function of time for the second GCM run.

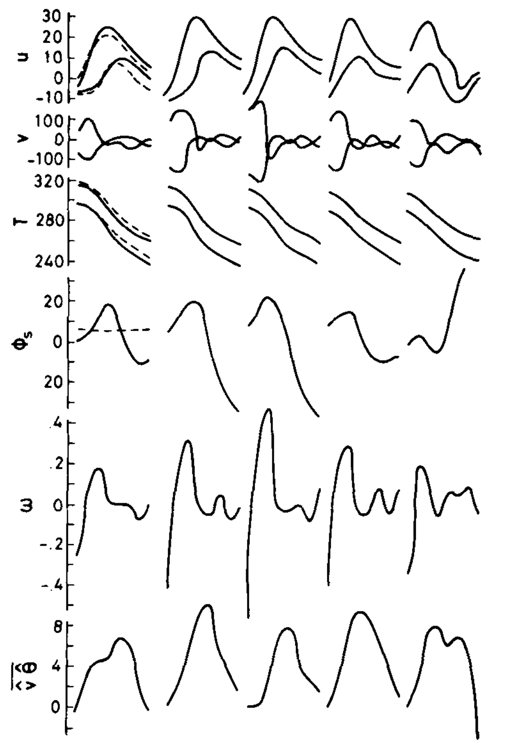

Fig. 12. Same as Fig. 5 except for second GCM run. The dashed lines show the initial state.

associated with 30-day averages, the perturbation forcing was increased to -1.2×10^{-5} K s^{-1} on the 3rd 30 days and then to -2.4 K s^{-1} for the last two 30-day periods for wave number 3. No forcing of waves 6, 9, and 12 was allowed after 90 days.

Fig. 12 shows the zonal averages for each successive 30 days. Note that basically the same zonal state results for this model as for the one with fewer meridional grid points. The major difference seems to be that the zonal wind looks qualitatively more reasonable and the meridional wind less reasonable. Note also that the zonal state stays fairly constant until the last 30 days at which point it becomes less realistic with easterlies appearing in high latitudes.

Fig. 13 shows the wave amplitudes as a function of latitude for each of the 30 days as compared to linear theory. Only wave number 3 is shown since after day 90 that was the only wave that was forced. Also, before then the amplitudes of the stationary waves from the linear model were much smaller for wave numbers 6, 9, and 12 than they were for wave number 3.

For the first 30 days linear theory is fairly accurate in describing the response. Basically, the negative cosine heating has a response in the negative sine of the potential temperature, meaning that it is warm downstream from the warm anomaly. The response is not well described by linear theory for the second 30 days presumably because of the additional noise induced in the system by the addition of more wave numbers. Therefore, the heating was increased by a factor of 5 for the third 30 days. Linear theory compares well with the average response for this third 30-day period. Increasing the heating to -2.4×10^{-5} K s^{-1} for the fourth 30 days doubles the response, but a wave in the cosine field is beginning to show up. On the fifth 30 days, when the forcing was the same as for the fourth 30 days, the linear model reaches a resonant state. That is, the zonal state of the GCM is such that the linear model will have large amplitude responses. The linear model results for this last period are divided by a factor of 3 in order to fit it on to the figure. Also note that the cosine wave has

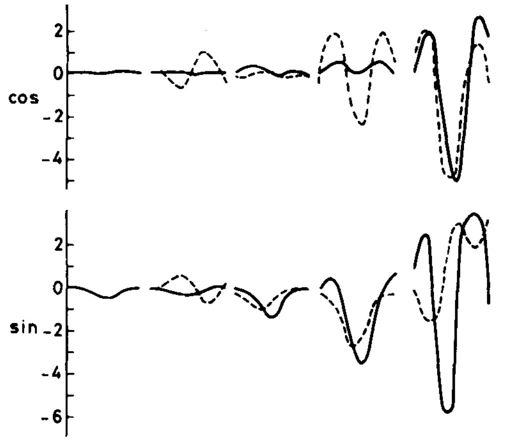

Fig. 13. Thirty day averages in 2nd GCM run (———) compared to linear theory (– – – –) as a function of grid points running from equator to pole. Each 30-day period is separated. Only the response in wave number 3 is shown. The liner model results for the last period are divided by a factor of 3. The ordinate units are degrees K.

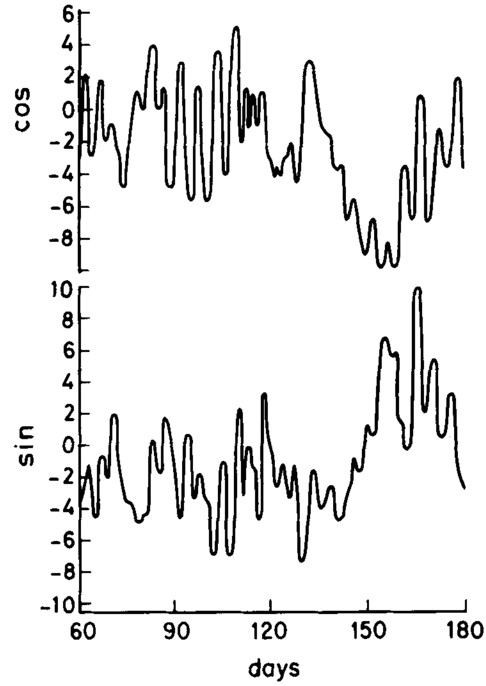

Fig. 14. Times series of the potential temperature at gridpoint four (~40° lat) for wave number 3. The upper curve is the cosine wave and the lower curve is the sine wave. Ordinate values are in K.

become extremely large indicating that the model is in a resonant growth period with positive heating producing positive temperatures. It was at this point the integration was stopped.

4.3. *Third GCM run*

The experiment was then repeated starting at day 60 with the forcing constant at -2.4×10^{-5} K s^{-1} for wave 3 (all other waves had zero forcings) throughout the next 4 months. Basically the same average values occur for the kinetic energy in the waves and zonal flow although toward the end (day 16) wave 3 obtains large kinetic energies (10^6 J m^{-2} s^{-2}) which then decrease once again. Fig. 14 shows a time series of wave number 3 at grid point 4 for the potential temperature. Even with constant forcing, the model has very short time scales and also long time scales.

Fig. 15 shows the comparison to linear theory during this time period. During the first two months, linear theory describes qualitatively the time averages. However, a similar situation develops in this third GCM run as was present in the second GCM run in that at the beginning of the third month the model moves slowly into a linear resonant state. The linear model results are divided by a factor of 3 only for the last experiment and hence it has taken somewhat longer for the third GCM run to move close to resonance. It should be noted that for this figure the forcing was kept constant. The different results occur because the time averaged zonal state is different for each 30-day run.

Summarizing, the last two GCM runs showed that in order to get large amounts of kinetic energy in the low wave numbers, one must include additional wave numbers beyond the most unstable wave. Once this was done, the noise in the time averaged solution for wave number 3 was so large that the anomalous forcing had to be increased substantially in order to make the linear solution stand out of the noise. This larger forcing resulted in predictability of monthly averages by linear theory for a while until the model went into linear resonance. The linear resonant state is characterized by having a large potential temperature response in phase with or slightly upstream from the heating, whereas the linear response far away from resonance is characterized by having a

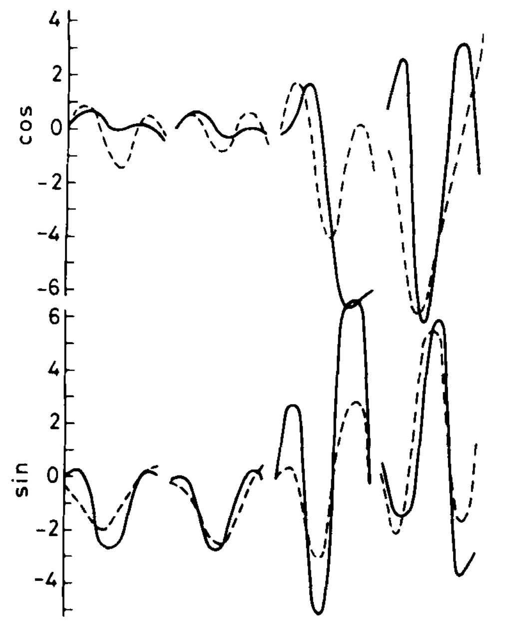

Fig. 15. Same as Fig. 13 except for third GCM run.

smaller amplitude response and the temperature high to the east of the heating by 90° of phase.

5. Conclusions

Stationary linear theory and a simple general-circulation model (GCM) were used to describe the atmospheric response in middle latitudes to local anomalies. The Fourier expansion of a locally anomalous heating gives equal amplitudes for all heating waves. However, the atmospheric response is dominated by the largest scale waves and then decreases for the smaller waves. In the linear model, which used the observed zonal state for an average winter, the response decreases as the inverse of the zonal wave number and can be explained by quasigeostrophic theory for the ultralong waves. That is, the perturbation heating is balanced by zonal advection of temperature. The response has warm lows downstream and cold highs upstream of a point-source heating.

Similar responses were obtained in the GCM with low truncation which had, in addition, a time-varying zonal and perturbation state, non-linear terms, additional heating feedbacks and horizontal smoothing. It was shown that the stationary linear model could be used to predict the anomalous response in the GCM for at least the largest scale waves. The waves which were associated with baroclinic instability had so much variation in their time-average state (average of 4 weeks) that meaningful comparisons between linear theory and the GCM could not be made for the shortest waves.

When the number of waves was increased to include smaller scale waves, the eddy kinetic energy and consequently noise in the largest scale waves increased; hence, the anomalous heating had to be made much larger in order to obtain a statistically significant result in short period integrations. Linear theory was shown to be able to describe the monthly averages until the model moved to a linear resonant state. At this point the linear model results were an order of magnitude larger than, but in phase with, the time averages of the GCM.

The linear model that was used to diagnose the GCM response in this paper was absolutely the same as the simple GCM, excepting the non-linear and transient perturbation fluxes. Further tests are suggested for GCM's that model the observed climate more accurately. Comparisons should be made with larger models that include orography, the hydrological processes, and the heating processes including the seasonal cycle with more rigorous parameterizations. Such experiments are planned for the future in order to understand complicated GCM answers to simple climatic questions.

6. Acknowledgements

This research has been supported by the National Science Foundation's Office of Climate Dynamics (ATM78-24003) and the International Decade of Ocean Exploration (OCE77-22882), and the Max Planck Institute of Theoretical Meteorology in Hamburg, F.R. Germany. The computer time was furnished in part by the National Center for Atmospheric Research, which is sponsored by the National Science Foundation, and in part by the Max Planck Institut of Theoretical Meteorology. I thank K. Hasselmann for inviting me to spend a few months there and also thank the various people who made the stay thoroughly enjoyable, especially G. Leipold and G. Hannoshöck. The work has been improved through discussions with T. Barnett, D. Cayan, and J. Namias of Scripps Institution of Oceanography, J. Egger at the University of Munich, and K. Hasselmann. L. Roads and E. Gaber typed the manuscript and Frau Voss drafted the figures. Finally, I thank the reviewers for their help in revising the paper.

7. Appendix I. Heating parameterizations

The heating parameterizations are taken from simple considerations of processes occurring on the earth. The relevant equations are:

$$\frac{\partial \theta}{\partial t} = \frac{g}{2\Delta p} C_p \{F_{s,s} + F_{L,s} + F_{r,s} - F_{1/2}\} \left(\frac{p_0}{p}\right)^{\kappa}$$

$$= A + BTg + C\theta + E\sigma$$

$$\frac{\partial \sigma}{\partial t} = \frac{g}{2\Delta p} C_p \{2F_{3/2} - F_{s,s} - F_{L,s} - F_{r,s} - F_{1/2}\} \left(\frac{p_0}{p}\right)^{\kappa}$$

$$= A_\sigma + B_\sigma Tg + C_\sigma \theta + E_\sigma \sigma$$

$$\frac{\partial Tg}{\partial t} = C_g^{-1} \{-F_{s,s} - F_{L,s} - F_{r,s}\}$$

$$= A_s + B_s Tg + C_s \theta + E_s \sigma$$

The coefficients A, B, C, E are obtained from linearizing various heating processes. From Smagorinsky (1963),

$$F_{r,s} = -(1 - A^*)(1 - \chi)(1 - A)\, u_0 S + \sigma Tg^4 - \nu\!\downarrow \sigma \theta^4$$

$$F_{1/2} = -uS(1 - A) + \nu\!\uparrow \sigma \theta^4 + (1 - \Gamma)\sigma Tg^4$$

$$F_{3/2} = (F_{r,s} + F_{1/2})/2$$

A simple bulk aerodynamic model is used to calculate the sensible heat,

$$F_{s,s} = \rho_s C_D |\mathbf{v}_s| (Tg - Ts)$$

Using a simple Bowen ratio

$$F_s = \frac{L}{C_p} \frac{\partial q^*}{\partial T} F_{s,s}$$

The frictional stress at the surface is

$$\tau_s = -\rho_s C_D |\mathbf{v}_s| \mathbf{v}_s = -k_s \mathbf{v}_s;\ k_s = 4 \times 10^{-6}\ \mathrm{s}^{-1}$$

It is now obvious how to derive the coefficients A, B, C, E, k_s. Because of the desire to make the comparisons between the linear and non-linear models as close as possible, the coefficients were kept constant during the course of the integrations. This seemed to be an adequate approximation for all variables excepting the static stability. Although, the average effect of the atmospheric motions is to stabilize the system, local variations in the vertical velocity can cause large changes in the stability. Normally, this is taken care of by a convective adjustment mechanism which seems to be related, for the most part, to cumulus clouds. This results in non-constant coefficients in the static stability equation. Hence, for this study, A_σ was set equal to 10^{-3} K s^{-1} and E_σ was set equal to -10^{-4} s^{-1}. Essentially, this results in σ being equal to 10 K or the potential temperature differs, between 400 and 800 mb, by 20 K.

Also, the frictional coefficient k_1, in the middle levels for the equation $(\partial \mathbf{v}/\partial t) = \pm k_1(\mathbf{v}_2 - \mathbf{v}_1)$, is set to 10^{-6} s. The other constants used in the model are,

$R = 2.87 \times 10^2$ J kg^{-1} K^{-1}
$C_p = 9.96 \times 10^2$ J kg^{-1} K^{-1}
$C_g^{-1} = 2.5 \times 10^{-6}$ m^2 J^{-1}
$g = 9.81$ m s^{-2}
$a = 6.37 \times 10^6$ m
$\Delta p = 400$ mb

For the second and third GCM runs, with 8 meridional grid points, the values are somewhat similar except $C_g^{-1} = 5 \times 10^{-6}$ m^2 J^{-1}.

8. Appendix II. Linear and nonlinear model comparisons

The differences between the GCM and the linear model can be represented as follows. First, the GCM can calculate the zonal solution. This zonal solution is used in the perturbation equation which is for the leap-frog step

$$\frac{\hat{x}^{n+1} - \hat{x}^{n-1}}{2\Delta t} = \frac{-\nabla^m \hat{x}^{n-1}}{2\Delta t} + (I - \nabla^m) \{-\bar{B}^n \hat{x}^n + \hat{X}^{n-1} - \sum \sum \hat{c}\hat{x}^n\}$$

and for the Euler step

$$\frac{\hat{x}^{n+1} - \hat{x}^n}{\Delta t} = \frac{-\nabla^m \hat{x}^n}{\Delta t} + (1 - \nabla^m)\{-\bar{B}\hat{x}^* + \widehat{X^n}$$

$$-\sum\sum \hat{c}^* \hat{x}^*\}$$

Combining the two equations into a time-average (denoted by $\sim$) by noting that the leap-frog time step is applied β times and the Euler-backward step α times gives

$$\frac{\beta\tilde{\hat{x}}^{n+1} - \beta\tilde{\hat{x}}^{n-1} + 2\alpha\tilde{\hat{x}}^{n+1} - 2\alpha\tilde{\hat{x}}^n}{2\Delta t} =$$

$$-\frac{\nabla^m 2\alpha\tilde{\hat{x}}^n + \beta\tilde{\hat{x}}^{n-1}}{2\Delta t}$$

$$+ (1 - \nabla^m)\begin{Bmatrix} -\beta\widetilde{\bar{B}^n\hat{x}^n} - \alpha\bar{B}^*\tilde{\hat{x}}^* + \beta\tilde{\hat{X}}^{n-1} + \alpha\tilde{\hat{X}}^n \\ -\beta\sum\sum\widetilde{\hat{c}^n\hat{x}^n} - \alpha\sum\sum\widetilde{\hat{c}^*\hat{x}^*} \end{Bmatrix}$$

The stationary model is now compared to the non-linear model by assuming

$$0 = \frac{(2\alpha + \beta)}{2\Delta t}\nabla^m\tilde{\hat{x}} + (1 - \nabla^m)(-\tilde{\bar{B}}\tilde{\hat{x}} + \tilde{\hat{X}})$$

One of the assumptions in this comparison is that

$$\beta\tilde{\hat{x}}^n + \alpha\tilde{\hat{x}}^* = \tilde{\hat{x}}^n$$

So far as can be discerned, the solution varies smoothly through the infrequent Euler-backward step, and so the above is assumed to be extremely accurate. Likewise, $\beta\tilde{\hat{x}}^{n+1} + \alpha\tilde{\hat{x}}^n = \hat{x}^n$ is also assumed accurate. The assumption

$$\frac{\beta\hat{x}^{n+1} - \beta\hat{x}^{n-1} + 2\alpha\hat{x}^{n+1} - 2\alpha\hat{x}^n}{2\Delta t} = 0$$

is valid if the time-averaging is done over a sufficiently long period of time. The other assumption of

$$\widetilde{B'\hat{x}'} + \sum\sum\widetilde{\hat{c}'\hat{x}'} - \sum\sum\tilde{\hat{c}}\tilde{\hat{x}} = 0$$

is not likely to be true, especially if the amplitudes of the perturbations are large.

REFERENCES

Arakawa, A. and Mintz, Y. 1974. The UCLA Atmospheric General Circulation Model. Department of Meterology. Univ. of Calif., Los Angeles, California.

Ashe, S. 1979. A nonlinear model of the time-average axially asymmetric flow induced by topography and diabatic heating. *J. Atmos. Sci. 36*, 109–126.

Chervin, R. M. and Schneider, S. H. 1976a. A study of the response of NCAR GCM climatological statistics to random perturbations: estimating noise levels. *J. Atmos. Sci. 33*, 391–404.

Chervin, R. M. and Schneider, S. H. 1976b. On determining the statistical significance of climate experiments with general circulation models. *J. Amos. Sci. 33*, 405–412.

Chervin, R. M., Washington, E. M. and Schneider, S. H. 1976. Testing the statistical significance of the response of the NCAR General Circulation Model to north Pacific Ocean surface temperature anomalies. *J. Atmos. Sci. 33*, 413–423.

Derome, J. and Wiin-Nielsen, A. 1971. Response of a middle latitude model atmosphere to forcing by topography and stationary heat sources. *Mon. Wea. Rev. 99*, 564–576.

Egger, J. 1976a. The linear response of a hemispheric two-level primitive equation model to forcing by topography. *Mon. Wea. Rev. 104*, 351–363.

Egger, J. 1976b. On the theory of the steady perturbations in the troposphere. *Tellus 28*, 381–389.

Egger, J. 1977. On the linear theory of the atmospheric response to sea surface temperature anomalies. *J. Atmos. Sci. 34*, 613–614.

Francis, P. E. 1975. The use of a multipoint filter as a dissipative mechanism in a numerical model of the general circulation of the atmosphere. *Quart. J. R. Met. Soc. 101*, 567–582.

Haltiner, G. J. 1971. *Numerical weather prediction.* John Wiley & Sons Inc., 317 pp.

Hasselmann, K. 1978. On the signal-to-noise problem in atmospheric response studies. *Archiv für Meterologie Geophysik und Bioklimatologie 27*, 251–259.

Herman, G. F. and Johnston, W. T. 1978. The sensitivity of the general circulation to Arctic sea ice boundaries: A numerical experiment. *Mon. Wea. Rev. 106*, 1649–1664.

Holton, J. R. 1972. An introduction to dynamical meteorology. *Academic Press.* New York.

Houghton, D. D., Kutzbach, J. E., McClintock, M. and Suchman, D. 1974. Response of a general circulation model to a sea temperature perturbation. *J. Atmos. Sci. 31*, 857–868.

Huang, J. C. K. 1978. Response of the NCAR general circulation model to North Pacific sea surface temperature anomalies. *J. Atmos. Sci. 35*, 1164–1179.

Julian, P. R. and Chervin, R. M. 1978. A study of the southern oscillation and Walker circulation phenomenon. *Mon. Wea. Rev. 106*, 1433–1451.

Kurihara, Y. 1965. On the use of implicit and iterative methods for the time integration of the wave equation. *Mon. Wea. Rev. 93*, 33–46.

Kurihara, Y. 1967. Numerical integration of a nine-level global primitive equation model formulated by the box method. *Mon. Wea. Rev. 95*, 509–530.

Kutzbach, J., Chervin, R. M., Houghton, D. D. 1977. Response of the NCAR general circulation model to prescribed changes in ocean surface temperature. Part 1: Mid-latitude changes. *J. Atmos. Sci. 34*, 1200–1213.

Leith, C. E. 1973. The standard error of time-average estimates of climatic means. *J. Appl. Met. 12*, 1066–1069.

Manabe, S. and Terpstra, T. B. 1974. The effects of mountains on the general circulation of the atmosphere as identified by numerical experiments. *J. Atmos. Sci. 31*, 3–42.

Namias, J. 1962. Influence of abnormal surface heat sources and sinks on atmospheric behaviour. Proc. Int'l Symp. on Numerical Weather Prediction, Tokyo, Nov. 7–13, 1960. *Publ. Met. Soc. Japan*, 615–629.

Oort, A. H. and Rasmusson, E. M. 1971. Atmospheric circulation statistics. NOAA Professional Paper 5, for sale by Supt. Documents, Government Printing Office, Washington, D.C. 20402, stock no. 0317-0045.

Rowntree, P. R. 1972. The influence of tropical east Pacific Ocean temperatures on the atmosphere. *Quart. J. Roy. Met. Soc. 98*, 290–321.

Rowntree, P. R. 1976a. Response of the atmosphere to a tropical Atlantic Ocean temperature anomaly. *Quart. J. Roy. Met. Soc. 102*, 607–625.

Rowntree, P. R. 1976b. Tropical forcing of atmospheric motions in a numerical model. *Quart. J. Met. Soc. 103*, 583–605.

Salmon, R. and Hendershott, M. C. 1975. Large-scale air-sea interactions with a simple general circulation model. *Tellus 28*, 228–242.

Saltzman, B. 1968. Surface boundary effects on the general circulation and macroclimate: A review of the theory of quasi-stationary perturbations in the atmosphere. The Causes of Climatic Change, *Meteor. Mongr. 30*, Am. Met. Soc., 4–19.

Sankar-Rao, M. 1970. On global monsoons—Further studies. *Tellus 22*, 648–654.

Schutz and Gates, 1971. Global Climatic Data for Surface 800 mb, 400 mb: January. Communications Department, Rand, 1700 Main Street, Santa Monica, California 90406, U.S.A.

Shukla, J. 1975. Effect of Arabian sea-surface temperature anomaly on Indian summer monsoon: A numerical experiment. *J. Atmos. Sci. 32*, 503–511.

Shapiro, R. 1970. Smoothing, filtering and boundary effects. *Rev. Geophys. Space Phys. 8*, 359–387.

Simpson, R. A. and Downey, W. K. 1975. The effect of a warm mid-latitude sea surface temperature anomaly on a numerical simulation of the general circulation of the southern hemisphere. *Quart. J. Roy. Met. Soc. 101*, 847–867.

Smagorinsky, J. 1963. General circulation experiments with the equations; I. The basic experiment. *Mon. Wea. Rev. 91*, 99–164.

Spar, J. 1973a. Some effects of surface anomalies in a global circulation model. *Mon. Wea. Rev. 101*, 91–100.

Spar, J. 1973b. Transequatorial effects of sea surface temperature anomalies in a global circulation model. *Mon. Wea. Rev. 101*, 554–563.

Spar, J. 1973c. Supplementary notes on sea surface temperature anomalies and model generated meteorological histories. *Mon. Wea. Rev. 101*, 767–773.

Spar, J. and Atlas, R. 1975. Atmospheric response to variations in sea-surface temperature. *J. Appl. Meteor. 14*, 1235–1245.

Vernekar, A. D. and Chang, H. D. 1978. A statistical-dynamical model for stationary perturbations in the atmosphere. *J. Atmos. Sci. 35*, 433–444.

Washington, W. M. 1972. Numerical climate change experiments: The effect of man's production of thermal energy. *J. Appl. Met. 11*, 768–772.

Webster, P. J. 1972. Response of the tropical atmosphere to local steady forcing. *Mon. Wea. Rev. 100*, 518–541.

Williams, J. 1975. The influence of snowcover on the atmospheric circulation and its role in climatic change: An analysis based on results from the NCAR global circulation model. *J. Appl. Met. 14*, 137–152.

Williams, J. and Washington, W. M. 1974. Simulation of the atmospheric circulation using the NCAR global circulation model with ice age boundary conditions. *J. Appl. Met. 13*, 305–317.

ЭКСПЕРИМЕНТЫ С КЛИМАТИЧЕСКИМИ АНОМАЛИЯМИ В СРЕДНИХ ШИРОТАХ НА ОСНОВЕ ГЛОБАЛЬНОЙ МОДЕЛИ

Двухуровенная сферическая линейная модель, основанная на примитивных уравнениях, используется для обсуждения реакции атмосферного поля геопотенциала на локальный нагрев в средних широтах. Показано, что наибольшего значения реакция приземного геопотенциала и потенциальнои температуры достигает для волнового числа один и убывает обратно пропорционально волновому числу для следующих нескольких волн. Реакция на нагрев приводит к образованию теплой ложбины вниз по течению и холодного гребня вверх по течению и может объясняться зональной адвекцией температуры, уравновешивающей возмущение в поле нагрева. Проведено несколько экспериментов с моделью общей циркуляции низкого порядка для изучения аномалий и дано сравнение с линейной моделью. Показано, что если шум в системе не на много больше линейного решения или если зональное состояние модели общей циркуляции не слишком близко к линейному резонансу, линейная теория может описать осредненные по времени поля в модели общей циркуляции.